ADVANCED OPTICAL MATERIALS
www.advopticalmat.de

Check for updates

Heliconical Cholesterics Endows Spatial Phase Modulator with an Electrically Customizable Working Band

Chun-Ting Xu, Bing-Hui Liu, Cheng Peng, Quan-Ming Chen, Peng Chen, Pei-Zhi Sun, Zhi-Gang Zheng, Yan-Qing Lu,* and Wei Hu**

Multidimensional and large-scale parallel manipulation of light, especially on-demand tailoring of the working frequency and spatial phase front, is highly pursued in modern optics. Here, broadband tunable planar optics is demonstrated by electrically driving the nanohelix of photopatterned heliconical cholesterics. By preprogramming the initial orientation of the helixes using a dynamic-mask photoalignment technique, spatial geometric phases can be arbitrarily encoded to the reflected light in a reconfigurable way. Due to the reversible electrically variant pitch of the heliconical superstructures, the reflective Bragg band can be precisely selected in the range from 380 to 1550 nm. In addition to wavelength selection and geometric phase modulation, spatial amplitude modulation and spin reversion can be further expected. This may offer a platform for full-dimensional manipulation of light, including wavelength/frequency, phase, amplitude, time, and spin, thus upgrading optical information processing techniques.

1. Introduction

Vital fields such as supercomputing, constellation satellite communication, 5G/6G communication, virtual/augmented reality, and holographic display have an increasing demand for information processing, transmission, and interaction with super large capacity and low power consumption. Compared to electronic information, which relies on the sequential or frequential modulation of electrical signals, photonic technology exhibits the natural advantages of multidimensional and large-scale parallel processing. However, the multidimensional correlation of wavelength/frequency, phase, amplitude, time, and polarization leads to the complexity of photon informatics. Accurate, efficient, and orthogonal manipulation of the multidimensional parameters of light thus becomes the core challenge for high-speed processing and reliable transmission of massive amounts of information. Recently, metasurfaces have broken the dependency of traditional optical elements on the propagation phase and significantly promoted the development of ultrathin planar optics.[1] Dielectric media are further adopted to eliminate the intrinsic loss of metals and improve the efficiency.[2] Broadband beam steering based on metasurfaces has been achieved.[3] Corresponding elements still suffer from static functions because their configurations cannot be varied once fabricated. Although various strategies, such as stretchable substrates,[4] phase-change materials,[5] and controlled chemical reactions,[6] have been introduced to develop actively tunable metasurfaces, it remains challenging to realize planar optics with on-demand working bands and functionalities, which are highly sought after in modern optics.

Liquid crystals (LCs) are considered excellent candidates for dynamic wavefront manipulation due to their excellent electro-optic properties.[7] LC on silicon[8] and photopatterned geometric phase optics[9] enable the accurate, arbitrary, and reconfigurable tilt and azimuthal angle control of LCs, supplying a powerful approach for the manipulation of light. However, the efficiency of the phase modulation is determined by the phase retardation for the widely used nematic LCs, thus leading to intensive wavelength dependency. Cholesteric LC (CLC), featuring a nano chiral helical structure, exhibits circular-polarization-selective Bragg reflection.[10] Light within the Bragg refection band and with the same helicity of CLC is reflected in equal efficiency. Meanwhile, a geometric phase is encoded by the photonic spin-orbit interaction of the space-variant initial orientation of the CLC helixes.[11,12] The light outside the band or with opposite helicity mostly transmits the CLC.[13] In addition to a broadband birefringence, CLC also exhibits stimuli responsiveness to temperature, light, magnetic/electric field, and so on.[14] Multiple external fields are adopted to trigger photonic bandgap tuning. For example, the thermal-driven continuous band shifting of CLC is utilized for wavelength-selective detection of the orbital angular momenta of light.[15] CLC doped with chiral optical molecular switches is demonstrated as

---

C.-T. Xu, C. Peng, Q.-M. Chen, P. Chen, Y.-Q. Lu, W. Hu
National Laboratory of Solid State Microstructures
Key Laboratory of Intelligent Optical Sensing and Manipulation
and College of Engineering and Applied Sciences
Nanjing University
Nanjing 210023, China
E-mail: yqlu@nju.edu.cn; huwei@nju.edu.cn

B.-H. Liu, P.-Z. Sun, Z.-G. Zheng
School of Physics
East China University of Science and Technology
Shanghai 200237, China
E-mail: zgzheng@ecust.edu.cn

The ORCID identification number(s) for the author(s) of this article can be found under https://doi.org/10.1002/adom.202201088.

DOI: 10.1002/adom.202201088

© 2022 Wiley-VCH GmbH

21951071, 2022, 19, Downloaded from https://advanced.onlinelibrary.wiley.com/doi/10.1002/adom.202201088 by Nanjing University, Wiley Online Library on [13/05/2025]. See the Terms and Conditions (https://onlinelibrary.wiley.com/terms-and-conditions) on Wiley Online Library for rules of use; OA articles are governed by the applicable Creative Commons License

light-activated working-band-tunable planar optics and quadridimensional manipulable lasers.[16,17] Compared with thermo and light tuning, electric field control is more favorable due to the merits of compactness, stability, and reliability. However, direct electric tuning of the Bragg band of CLC is elusive due to the strong perturbation of the helical structure under the electric field.[18] Dual-frequency LC and ferroelectric LC doped with chiral dopants are driven by a specific electric field to change the temperature and thus tune the Bragg band accordingly.[19,20] A polymer stabilization and wash-out-refill strategy is adopted to achieve an electrically tunable working band of CLC planar optics.[21,22] However, these techniques suffer from a limited tuning range of wavelength or a high electric field. Therefore, planar optics with arbitrary wavefront manipulation and ultrabroadband wavelength selectivity is still an urgent pursuit.

The heliconical cholesterics, although predicted more than half a century ago,[23] were discovered very recently in bent-shaped LC dimeric compounds.[24–27] It has attracted intensive attention due to the broadband tunable reflective band derived from the electric-driven pitch variation of its nanohelix. Spatial amplitude modulation was accomplished by the light-driven state transition of optically responsive heliconical cholesterics.[27] Spatial phase modulation is also expected in the same system. However, biaxiality results in disclinations,[26,27] leading to nonuniform colors and uncontrollable phase interruptions. This severely hinders the utilization of heliconical cholesterics in phase front modulation. In this work, we drastically improve the domain uniformity on the bases of noncontact photoalignment[28] and an optimized electrical driven method. Thereby, photopatterned heliconical cholesterics are demonstrated as geometric-phase planar optics with customizable working frequency covering the near-UV, visible till near-IR bands for the first time. Point-to-point photoalignment technology enables rewritable, high-quality, and high-resolution prealignment and subsequent self-organization of heliconical superstructures and thus can realize free and large-scale parallel geometric phase encoding in a reconfigurable way. Under an applied normal electric field, directors of heliconical cholesterics tilt toward helical axes, and the pitch reduces. Correspondingly, the reflection band blue shifts from 1550 to 380 nm with a continuously narrowed width. The electrical band selectivity of the optical vortex (OV) generator, beam deflector, and lens are presented. This releases the freedom for both spatial phase modulation and working frequency customization of planar optics. It will upgrade present optical systems and inspire wide applications in mode/wavelength multiplexing optical communications, all optical networks, hyperspectral imaging, and holographic displays.

2. Results and Discussion

Here, the material is bimesogenic LC (CB7CB) and left-handed chiral dopant (S811) (**Figure 1**a) mixed in nematic LC (E7). CB7CB is characterized by two cyanobiphenyl mesogens connected by a flexible chain with an odd number of carbons. Its bend elastic constant K_3 is smaller than the twist elastic constant K_2. Therefore, the heliconical superstructures can remain stable under an electric field. Figure 1b illustrates the structural evolution of a homogenously aligned sample under different electric fields. The cell gap of the sample is 12 μm. Figure 1b-i reveals a helicoidal state with $\theta = 90°$ when the field is below E_1 (0.3 V μm^{-1}, Text S1, Supporting Information). Actually, focal conic domains exist because the helicoidal superstructures of the bimesogenic mixture cannot be uniformly aligned by only azimuthal angle control. When the field is between E_1 and E_2 (2.5 V μm^{-1}, Text S1, Supporting Information), the LC director tilts toward the helical axis with a field-dependent angle θ. As depicted in Figure 1b-ii–iv, the helical pitch P decreases with increasing applied field. Consequently, the reflective band blueshifts in an ultrabroad range from 1550 to 380 nm, corresponding to near-IR, visible, and near-UV bands (Figure 1c). The tunable range of the heliconical superstructures (>1100 nm) is much larger than that of other CLC superstructures (≤300 nm),[12,20,22] and the driving voltage is lower (≤3 V μm^{-1}). In addition, the bandwidth of the Bragg reflection band (≤20 nm) is much narrower in the visible region, which enables better wavelength selectivity. For efficiency, it is slightly lower than traditional CLC ones. Moreover, the bandwidth continuously narrows due to the reduced birefringence Δn with decreasing θ (Figure S2, Supporting Information). When a strong electric field beyond E_2 is applied, a homeotropic state emerges (Figure 1b-v). Figure 1d presents the micrographs recorded under a polarization optical microscope (POM) with a pair of crossed polarizers. The electric field decreases directly from 3 V μm^{-1} to target voltages to form a uniform domain structure. A dark homeotropic state is observed at the beginning, and uniform purple, blue, green, yellow, orange, and red reflective colors are successively observed under different fields. Finally, the sample recovers to the initial focal conic domains when the field is absent. The process is reversible and repeatable.

Since ultrabroadband selectivity is demonstrated, various planar optics with on-demand tunable frequencies are expected. An OV, characterized by a helical phasefront, carries orbital angular momentum (OAM) of $m\hbar$, where m is the topologic charge.[29] Due to the theoretically infinite number of OAM states, OVs can be used as carriers of information, by which the capacity of optical communication systems can be drastically enhanced via mode-division multiplexing.[30] A compact and efficient method for OAM processing compatible with traditional wavelength-division multiplexing (WDM) is in high demand. Here, we imprint the alignment orientation α of a q-plate,

$$\alpha_{q\text{-plate}} = q\theta + \alpha_0 \tag{1}$$

where $q = m/2$ and set as 1 here, α_0 is the initial angle and set as 0 here, into the prealignment of a heliconical CLC cell. Thus, a geometric phase of $\pm 2\alpha$ can be generated, depending on the chirality of heliconical superstructures. The specific space-variant orientation of the q-plate is implemented by sys with a multistep and partly overlapping exposure process.[31] As shown in **Figure 2**a, LC directors follow the guidance of local alignment and form the desired heliconical superstructures. A supercontinuum laser is filtered by a multichannel acousto-optic tunable filter to generate arbitrary monochromatic wavelengths in the range of 410–1200 nm. The polarization of the laser is then changed to left circular polarization by adjusting a

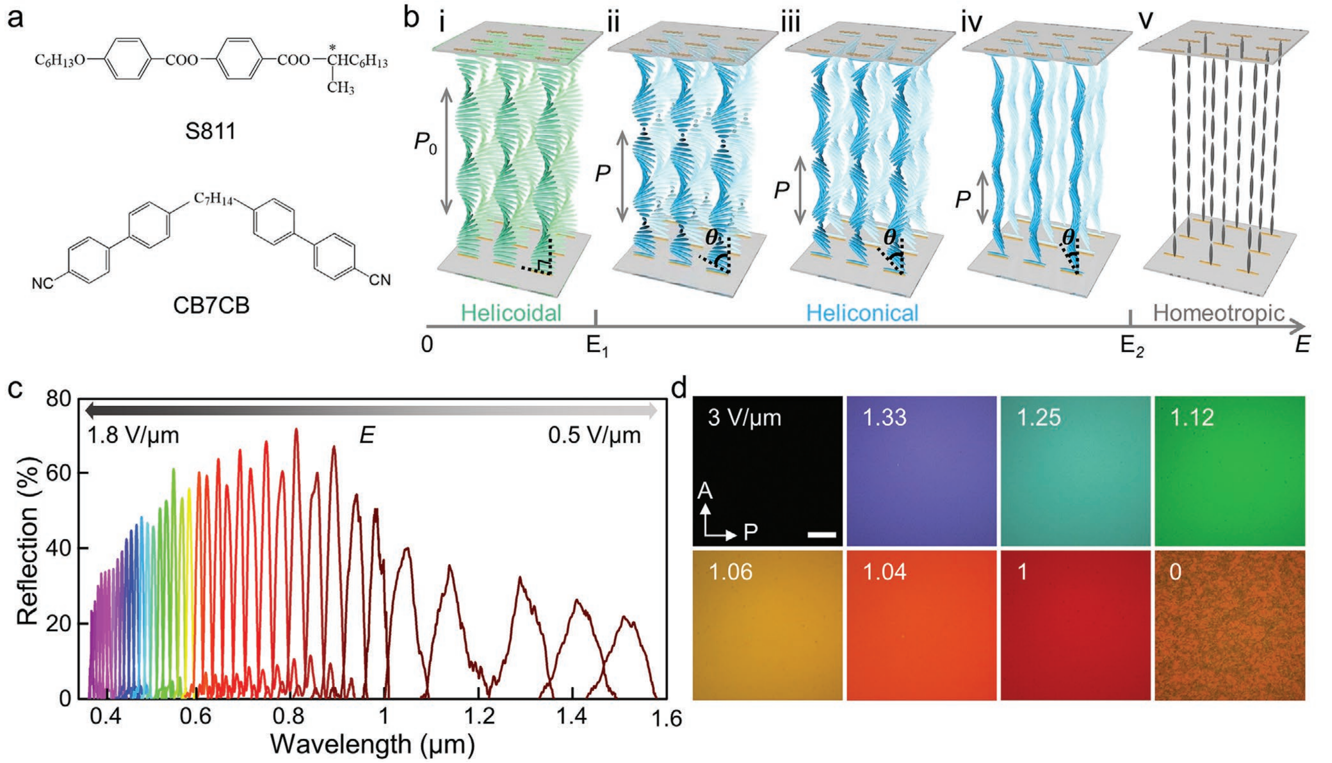

Figure 1. Helix transformation and performance of heliconical cholesterics under an electric field. a) Chemical structures of S811 and CB7CB. b) Schematic illustration of the helical superstructure transformation under different external electric fields. i) Helicoidal superstructure with LC director perpendicular to the helical axis, $E < E_1$; ii–iv) Heliconical superstructures with LC director oblique to the helical axis, in which the oblique angle θ gradually decreases as the electric field increases, $E_1 < E < E_2$; v) The unwound homeotropic nematic state with LC director parallel to electric field, $E > E_2$. E_1 and E_2 are the thresholds of the transition from the helicoidal state to the heliconical state and the heliconical state to the homeotropic state. c) Bragg reflection spectra under incident circular-polarization light and d) POM textures of homogenously aligned LC with different electric fields applied. The temperature of the cell is fixed at 26 °C. The scale bar indicates 200 µm for all micrographs.

linear polarizer and a broadband quarter waveplate. A nonpolarizing beam splitter is used to conveniently detect the reflected beam (Figure 2b). As shown in Figure 2c, dark Maltese crosses are observed in all micrographs due to the space-variant orientation of the heliconical superstructures. The color variation among textures under different fields (1.31, 1.2, 1.09, 1.08, 1.01, and 0.95 V μm^{-1}) is consistent with previous homogeneously aligned ones. The corresponding reflected OVs exhibit donut-like intensity profiles and verify the excellent wavelength selectivity over a wide range from 458 to 820 nm. A cylindrical lens is placed before the CCD, and the CCD is fixed exactly at the focal plane to detect the topologic charge. In Figure 2d, the number of dark branches and the tilt direction of the strips indicate $m = +2$, which matches the original design well.[32] OAM mode generators show a low-voltage controlled and ultrabroad tunable working band, which enables WDM-compatible OAM processing that may be widely used in optical communications and quantum informatics.

Diffraction grating is a typical optical element widely used in beam steering and spectroscopy. Polarization grating (PG) features a periodic and gradient phase change between 0 and 2π, whose alignment orientation is expressed as follows:

$$\alpha_{\mathrm{PG}} = -\frac{\pi x}{\Lambda} + \alpha_o \tag{2}$$

Here, Λ is the period of the PG and is set as 100 µm, and α_0 is still set as 0 here. It exhibits a theoretical diffraction efficiency up to 100%.[33] **Figure 3**a shows the theoretical director distribution diagram and schematic illustration of a heliconical PG. The micrograph of the sample under 1.24 V μm^{-1} vividly reveals the periodic brightness change along the grating director. Along with the structural evolution driven by the electric field (Figure S3a, Supporting Information), the wavelength of the reflectively deflected beam is continuously tuned, as presented in Figure 2b.

The slight voltage variation between the q-plate and PG is attributed to the different impedance and voltage division factors among different homemade cells. It is expected to be successfully eliminated via a mature production process. The deflection angle increases with the selected wavelength, and the exact value can be obtained according to the grating equation. An intensive circular polarization (spin) dependency is exhibited thanks to the chiral configuration of the heliconical superstructure. Light of the same helicity and within the Bragg refection is selectively reflected in high efficiency. The average efficiency of the 0th order (mirror and unconverted Gaussian beam reflections) is 20.7 ± 4.9%. The average efficiency of the –1st order is 2.8 ± 0.5%, which is highly suppressed due to the spin selectivity of heliconical cholesterics. The average efficiency of the +1st order reaches over 72% in the whole visible

© 2022 Wiley-VCH GmbH

21951071, 2022, 19, Downloaded from https://advanced.onlinelibrary.wiley.com/doi/10.1002/adom.202201088 by Nanjing University, Wiley Online Library on [13/05/2025]. See the Terms and Conditions (https://onlinelibrary.wiley.com/terms-and-conditions) on Wiley Online Library for rules of use; OA articles are governed by the applicable Creative Commons License

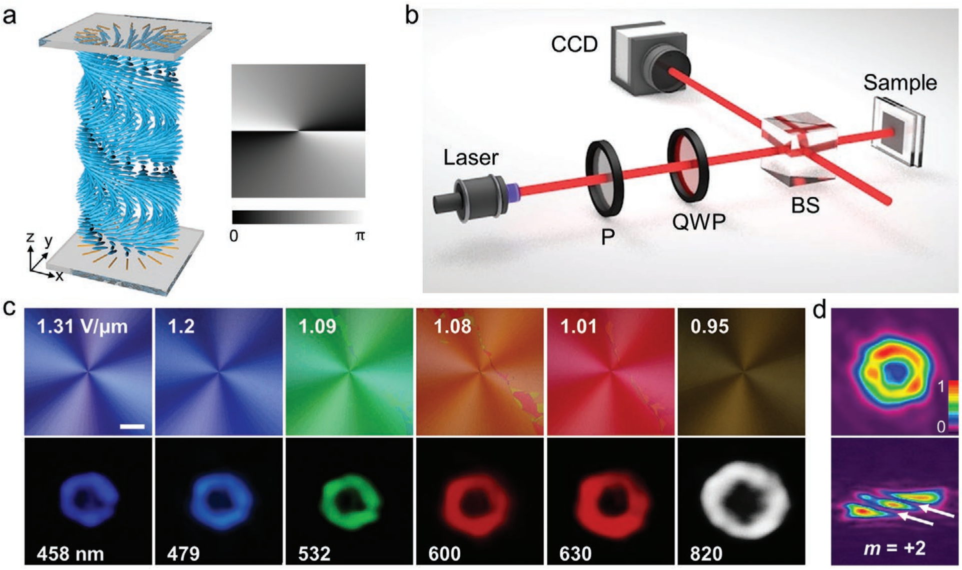

Figure 2. Broadband working characteristics characterization of OVs from the designed heliconical superstructures. a) Schematic illustration and theoretical director distribution of the q-plate with $q = 1$. Black to white indicates the direction changing from 0° to 180°. b) Scheme of the experimental setup. P, linear polarizer; QWP, quarter waveplate; BS, nonpolarizing beam splitter; CCD, charge-coupled device. c) Micrographs and corresponding reflected optical vortices under different electric fields. d) Reflected optic vortex and corresponding OAM detection. The scale bar indicates 200 μm for all micrographs.

band (Figure 3c). In contrast, the efficiency of light with opposite helicity and outside the Bragg band is mostly depressed, and this part of light transmits through the sample directly (Figure S3b, Supporting Information). The performance of the proposed grating is distinct from that of traditional gratings. As shown in Figure 3d, different frequency channels are selectively

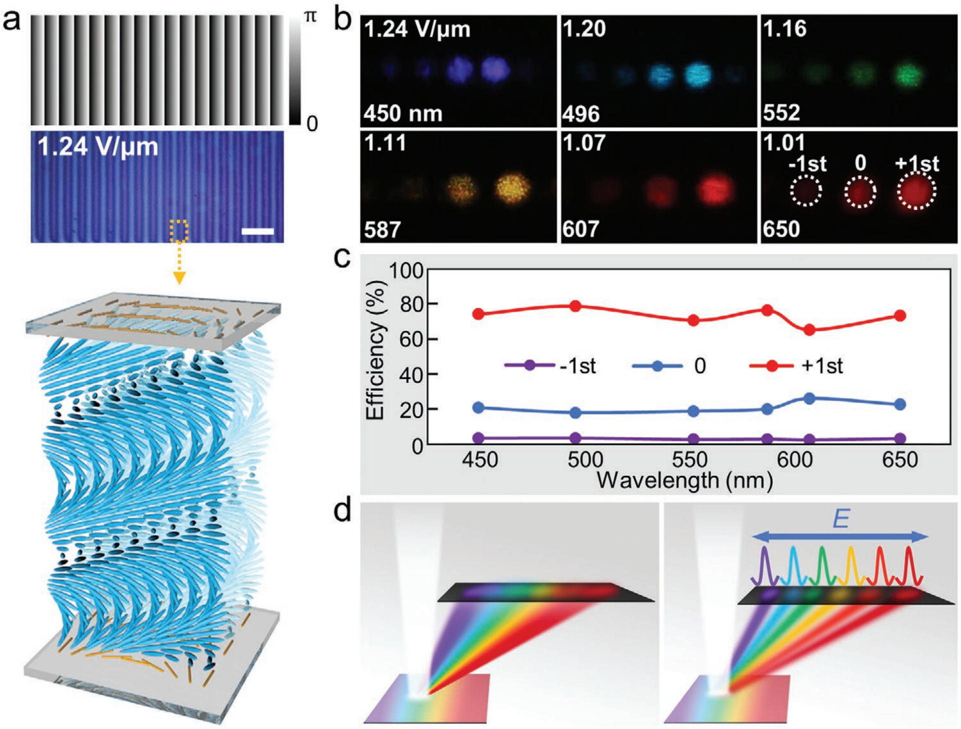

Figure 3. Experimental demonstration of broadband tuning by a fabricated heliconical PG. a) Theoretical director distribution, POM micrograph, and schematic illustration of PG. Black to white indicates the direction changing from 0° to 180°. b) Diffractive intensity distributions and c) wavelength-dependent diffraction efficiencies of PG. d) Schematic diagrams of the traditional grating and the proposed band-selective PG. The scale bar indicates 200 μm for all micrographs.

21951071, 2022, 19, Downloaded from https://advanced.onlinelibrary.wiley.com/doi/10.1002/adom.202201088 by Nanjing University, Wiley Online Library on [13/05/2025]. See the Terms and Conditions (https://onlinelibrary.wiley.com/terms-and-conditions) on Wiley Online Library for rules of use; OA articles are governed by the applicable Creative Commons License

deflected to a wavelength-dependent angle, while traditional gratings disperse all input light simultaneously. Moreover, the heliconical PG is spin dependent, adding an extra degree of freedom to dynamically manipulate the functions. Such PG may be utilized in augmented reality displays,[34] all optical networks and laser communications with the capability of dynamic wavelength channel control.

Due to the rewritability of the photoalignment agent, the predefined patterns could be reconfigurable via an erasing and then photoalignment process at the homeotropic or isotropic state. To eliminate the influence of the CLC, the rewriting process is carried out when the sample is driven to a homeotropic state with an electric field of 3 V µm^{-1}; otherwise, the sample is kept in an isotropic state by heating the sample over the clearing point. Due to the rewritability of the azo dye, the initial pattern will be erased and rewritten simultaneously by recording a new pattern under the digital micromirror device (DMD)-based dynamic photopatterning system after an exposure dose of 5 J cm^{-2},[7] and after cooling to the CLC state, the orientation will be reconfigured accordingly. Herein, the heliconical CLC is rewritten with an off-axis lens design, whose alignment orientation is expressed as follows:

$$\alpha_{\text{off-axis lens}} = \alpha_{\text{PG}} - \frac{\pi}{\lambda}\left(\sqrt{f^2 + r^2 - f}\right) + \alpha_{\text{o}} \tag{3}$$

The first and second terms represent the orientation introduced by the phase profiles of a PG and a lens,[35] respectively, while α_0 is still set as 0. Here, f is the focal length, λ is the wavelength of light, and r is the radial distance. The generation of the director distribution is illustrated in **Figure 4**a. An off-axis lens with $f = 13.5$ cm at 488 nm is fabricated for demonstration.

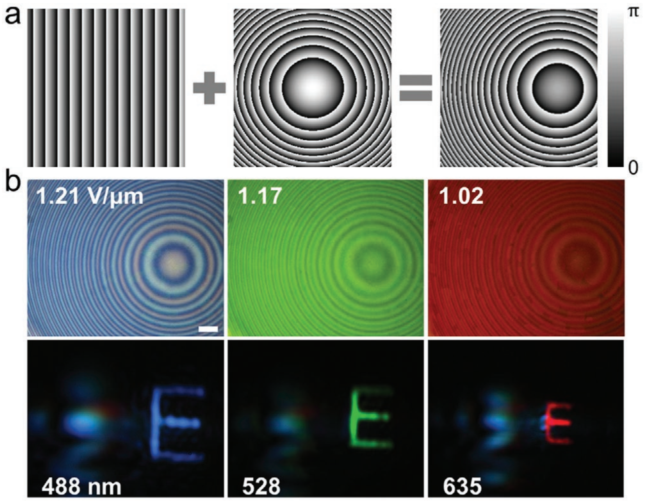

Figure 4. Design and characterization of a reconfigured off-axis lens based on heliconical cholesterics. a) The director distribution of the off-axis lens, which is the superposition of director distributions of a polarization grating and a lens. Black to white indicates the direction changing from 0° to 180°. b) Microphotographs of the off-axis lens with different electric fields applied and corresponding images of the letter "E" selected at central wavelengths of 488 (blue), 528 (green), and 635 nm (red) when lasers with three wavelengths are incident simultaneously. The scale bar indicates 200 µm for all micrographs.

As revealed in Figure 4b, patterns consistent with the designed off-axis lens are observed in all micrographs due to the space-variant orientation of the heliconical superstructures. The color variation among textures under different fields results from the change in P during structural evolution. A setup is built to characterize the imaging performance (Figure S4, Supporting Information). A letter "E" is placed farther than a focal length before the off-axis lens. The aperture size is 2 mm. Beams with wavelengths of 488, 528, and 635 nm are simultaneously incident to the off-axis lens. Images of object "E" are captured by a CCD. Only light with a selected wavelength and helicity can be focused to form an image. As shown in Figure 4b, blue, green, and red letters "E" are imaged under fields of 1.21, 1.17, and 1.02 V µm^{-1}, respectively. Due to the contribution of the PG component, the image is diffracted to a single 1st order. In this case, the crosstalk from the 0th-order reflection is totally avoided, making the images clearer. The switching time is on the scale of seconds. According to the relationship $1/v + 1/u = 1/f$, where v, u, and f are the image distance, object distance, and focal length, respectively, the larger the wavelength is, the smaller the image size. In the test, $u = 20$ cm is fixed, and $v = 41$, 34.5, and 23 cm, $f = 13.5$, 12.5, and 10.5 cm for $\lambda = 488$, 528, and 635 nm, respectively. The measured efficiencies of the off-axis lens for 488, 528, and 635 nm are 67.9%, 70.1%, and 68.2%, respectively. The broadband wavelength selectivity is promising in hyperspectral imaging and holographic displays.

For easy demonstration, three typical geometric phases of the q-plate, PG, and lens are encoded to the heliconical cholesterics. Since the utilized dynamic-mask photoalignment technique is suitable for large-scale (here 1920 × 1080, and larger one can be realized with a splicing process) and high-quality hierarchical architecting, more complicated spatial phases can be tailored and reconfigured arbitrarily. It enables a free and dynamic geometric phase modulation that can meet the broad requirement of planar optics. Due to the unique electric-driven P-variation of the heliconical superstructures, on-demand Bragg band (wavelength/frequency) selectivity is realized over a wide range from near-UV to near-IR bands. Although only wavelength selection and geometric phase modulation are demonstrated, spatial amplitude modulation and spin reversion can be expected as well. For a given wavelength, the amplitude can be spatially modulated by tuning the reflection band shift with patterned electrodes.[22] It perfectly meets the requirements of virtual/augmented realities. Additionally, pixelated spin selectivity can be realized by optically addressing a heliconical cholesteric doped with light-driven handedness-reversible chiral molecular switches (ChAD-3C-S, for instance).[16] The handedness of the chiral structure can be optically reversed by violet light or green light irradiation. The photoisomerization leads to a helical twisting power variation and thus flips the reflected circular polarizations. All of the above parameters of light (phase, frequency, amplitude, and polarization) can be dynamically (time) and orthogonally manipulated in a large-scale parallel way. Thus, the proposed technique meets the miniaturization, integration, adaptive, and dynamic-function tendencies of modern optics and supplies a practical platform for multidimensional and large-scale parallel light modulation. The working wavelength may be further broadened to the telecomm band by

© 2022 Wiley-VCH GmbH

21951071, 2022, 19, Downloaded from https://advanced.onlinelibrary.wiley.com/doi/10.1002/adom.202201088 by Nanjing University, Wiley Online Library on [13/05/2025]. See the Terms and Conditions (https://onlinelibrary.wiley.com/terms-and-conditions) on Wiley Online Library for rules of use; OA articles are governed by the applicable Creative Commons License

optimizing the concentration of the chiral dopant. The diffraction efficiency can be further increased by reducing impurities and defects.

3. Conclusion

We proposed heliconical cholesterics-based planar optics that is suitable for multidimensional light modulation. On-demand tailoring of the geometric phase and working frequency is demonstrated by photopatterning the heliconical superstructures and electrically tuning the helical pitches, respectively. An OV generator, beam deflector, and off-axis lens with ultrabroad wavelength selectivity covering the near-UV, visible till near-IR bands are presented. It releases the freedom for spatial phase modulation and working frequency selection of planar optics simultaneously. In addition, the feasibilities of spatial amplitude modulation, spin conversion, and sequential modulation are reasonably discussed. The photopatterned heliconical cholesterics thus provide a promising strategy for planar optics with merits of excellent flexibility, low cost, and easy fabrication. This work enriches the fundamental understanding of soft matter photonics and drastically extends the functionality of LC devices. It will upgrade present optical systems and inspire wide applications in optical computing, optical communications, hyperspectral imaging, virtual/augmented reality, and holographic displays.

4. Experimental Section

Materials: The heliconical CLC mixture was composed of bimesogenic LC (CB7CB, homemade), nematic LC (E7, HCCH, China), and left-handed chiral dopant (S811, HCCH, China) in weight proportion E7:CB7CB:S811 = 53.2:43.8:3. The mixture was magnetically stirred at 100 °C with a speed of 1000 rpm for 10 min. Its transition temperature from the homochiral nematic twist bend phase to the cholesteric phase was 18 °C, and the clearing point was 75 °C.

Cell Preparation and Photoalignments: Indium-tin-oxide glass substrates (1.5×2 cm^2) were ultrasonically bathed, UV-ozone cleaned, and then spin-coated with SD1 (Dai-Nippon Ink and Chemicals, Japan). After curing at 100 °C for 10 min, two pieces of glass substrates were assembled to form a 12-µm-thick cell with epoxy glue. The cell gap for all devices was 12 µm. Afterward, a DMD-based microlithography system[36] was employed to transfer the pattern into LC cells. Every region with directors varying from 0 to π was replaced by 18 equal subregions. Each subregion was endowed with a uniform director value, from $\pi/18$ to π in intervals of $\pi/18$. A sum of five adjacent subregions (i.e., the sum-region) was exposed simultaneously. Finally, each subregion was exposed five times with a total exposure dose of 5 J cm^{-2} that was sufficient to reorient the SD1 molecules. The subsequent exposure of the sum-region shifted one subregion with the polarizer rotating 10° synchronously. After the 18-step 5-time partly overlapping exposure, a quasi-continuous space-variant orientation of SD1 was carried out.[37]

Characterizations: The temperature was controlled at 26 °C by a hot stage (Linkam LTS 120, UK) in the experiment. A supercontinuum laser (SuperK EVO, NKT Photonics, Denmark) combined with a multichannel acousto-optic tunable filter (SuperK SELECT, NKT Photonics, Denmark) was adopted to output monochromatic or multicolor lasers. All micrographs were recorded under a POM (Nikon 50i POL, Japan). The reflection spectra in the visible region were measured with a spectrometer (PG2000-Pro, Ideaoptics, China). The reflection spectra in the near-UV region were measured with a spectrometer model (NOVA, Ideaoptics, China) paired with a light source (iDH2000, Ideaoptics, China). A supercontinuum source (SuperK EHtreme, NKT Photonics, Denmark) and an optical spectrum analyzer (AQ6370C, Yokogawa, Japan) were employed to measure the reflection spectra in the near-IR region. Diffraction patterns were captured by a digital camera (EOS M, Canon, Japan) or a CCD (DCC1645C-HQ, Thorlabs, USA). A 3 kHz square-wave AC signal was applied to electrically drive the samples. The signal was output by a function generator (33522B, Agilent Technologies Inc., USA) and amplified by a voltage amplifier (2340, TEGAM, USA).

Supporting Information

Supporting Information is available from the Wiley Online Library or from the author.

Acknowledgements

C.T.X., B.H.L., and C.P. contributed equally to this work. This work was supported by the National Key Research and Development Program of China (No. 2021YFA1202000), the National Natural Science Foundation of China (NSFC) (62035008, 61922038, and 62175101), Natural Science Foundation of Jiangsu Province, Major Project (BK20212004), and Fundamental Research Funds for the Central Universities (021314380189). The authors gratefully thank Dr. Yi-Feng Xiong for his kind assistance with the use of the facilities.

Conflict of Interest

The authors declare no conflict of interest.

Data Availability Statement

The data that support the findings of this study are available from the corresponding author upon reasonable request.

Keywords

geometric phase, heliconical cholesterics, photoalignment, planar optics

Received: May 11, 2022
Revised: June 28, 2022
Published online: August 4, 2022

---

[1] a) N. F. Yu, P. Genevet, M. A. Kats, F. Aieta, J. P. Tetienne, F. Capasso, Z. Gaburro, *Science* **2011**, *334*, 333; b) S. L. Sun, Q. He, S. Y. Xiao, Q. Xu, X. Li, L. Zhou, *Nat. Mater.* **2012**, *11*, 426; c) W. W. Wan, J. Gao, X. D. Yang, *ACS Nano* **2016**, *10*, 10671.
[2] a) D. M. Lin, P. Y. Fan, E. Hasman, M. L. Brongersma, *Science* **2014**, *345*, 6194; b) A. Arbabi, Y. Horie, M. Bagheri, A. Faraon, *Nat. Nanotechnol.* **2015**, *10*, 937; c) M. Khorasaninejad, W. T. Chen, R. C. Devlin, J. Oh, Y. Zhu, F. Capasso, *Science* **2016**, *352*, 1190.
[3] a) S. Wang, P. C. Wu, V. C. Su, Y. C. Lai, C. H. Chu, J. W. Chen, S. H. Lu, J. Chen, B. Xu, C. H. Kuan, T. Li, S. Zhu, D. P. Tsai, *Nat. Commun.* **2017**, *8*, 187; b) S. Wang, P. C. Wu, V. C. Su, Y. C. Lai, M. K. Chen, H. Y. Kuo, B. H. Chen, Y. H. Chen, T. T. Huang, J. H. Wang, R. M. Lin, C. H. Kuan, T. Li, Z. Wang, S. Zhu, D. P. Tsai, *Nat. Nanotechnol.* **2018**, *13*, 227; c) R. J. Lin, V. C. Su, S. Wang,

© 2022 Wiley-VCH GmbH

21951071, 2022, 19, Downloaded from https://advanced.onlinelibrary.wiley.com/doi/10.1002/adom.202201088 by Nanjing University, Wiley Online Library on [13/05/2025]. See the Terms and Conditions (https://onlinelibrary.wiley.com/terms-and-conditions) on Wiley Online Library for rules of use; OA articles are governed by the applicable Creative Commons License

M. K. Chen, T. L. Chung, Y. H. Chen, H. Y. Kuo, J. W. Chen, J. Chen, Y. T. Huang, *Nat. Nanotechnol.* **2019**, *14*, 227.

[4] a) S. C. Malek, H. S. Ee, R. Agarwal, *Nano Lett.* **2017**, *17*, 3641; b) A. She, S. Y. Zhang, S. Shian, D. R. Clarke, F. Capasso, *Sci. Adv.* **2018**, *4*, eaap9957.

[5] a) Q. Wang, E. T. Rogers, B. Gholipour, C. M. Wang, G. Yuan, J. Teng, N. I. Zheludev, *Nat. Photonics* **2016**, *10*, 60; b) X. Yin, T. Steinle, L. Huang, T. Taubner, M. Wuttig, T. Zentgraf, H. Giessen, *Light: Sci. Appl.* **2017**, *6*, e17016.

[6] J. X. Li, S. Kamin, G. X. Zheng, F. Neubrech, S. Zhang, N. Liu, *Sci. Adv.* **2018**, *4*, eaar6768.

[7] B. Y. Wei, W. Hu, Y. Ming, F. Xu, S. Rubin, J. G. Wang, V. Chigrinov, Y. Q. Lu, *Adv. Mater.* **2014**, *26*, 1305198.

[8] Z. Zhang, Z. You, D. Chu, *Light: Sci. Appl.* **2014**, *3*, e213.

[9] P. Chen, L. L. Ma, W. Duan, J. Chen, S. J. Ge, Z. H. Zhu, M. J. Tang, R. Xu, W. Gao, T. Li, W. Hu, Y. Q. Lu, *Adv. Mater.* **2018**, *30*, 1705865.

[10] I. C. Khoo, S. T. Wu, *Optics and Nonlinear Optics of Liquid Crystals*, World Scientific, Singapore **1993**.

[11] a) R. Barboza, U. Bortolozzo, M. G. Clerc, S. Residori, *Phys. Rev. Lett.* **2016**, *117*, 053903; b) M. Rafayelyan, G. Tkachenko, E. Brasselet, *Phys. Rev. Lett.* **2016**, *116*, 253902.

[12] J. Kobashi, H. Yoshida, M. Ozaki, *Nat. Photonics* **2016**, *10*, 389.

[13] P. Yeh, C. Gu, *Optics of Liquid Crystal Displays*, Wiley, New York **1999**.

[14] a) Z. G. Zheng, Y. N. Li, H. K. Bisoyi, L. Wang, T. J. Bunning, Q. Li, *Nature* **2016**, *531*, 352; b) H. K. Bisoyi, T. J. Bunning, Q. Li, *Adv. Mater.* **2018**, *30*, 1706512; c) R. S. Zola, H. K. Bisoyi, H. Wang, A. M. Urbas, T. J. Bunning, Q. Li, *Adv. Mater.* **2019**, *31*, 1806172; d) H. K. Bisoyi, Q. Li, *Chem. Rev.* **2022**, *122*, 4887.

[15] Y. H. Zhang, P. Chen, C. T. Xu, L. Zhu, X. Y. Wang, S. J. Ge, W. Hu, Y. Q. Lu, *ACS Photonics* **2022**, *9*, 1050.

[16] P. Chen, L. L. Ma, W. Hu, Z. X. Shen, H. K. Bisoyi, S. B. Wu, S. J. Ge, Q. Li, Y. Q. Lu, *Nat. Commun.* **2019**, *10*, 2518;

[17] H. L. Hu, B. H. Liu, M. Q. Li, Z. G. Zheng, W. H. Zhu, *Adv. Mater.* **2022**, *34*, 2110170.

[18] Z. G. Zheng, Y. Q. Lu, Q. Li, *Adv. Mater.* **2020**, *32*, 1905318.

[19] R. Chen, Y. H. Lee, T. Zhan, K. Yin, Z. W. An, S. T. Wu, *Adv. Opt. Mater.* **2019**, *7*, 1900101.

[20] S. A. Jiang, C. C. Lai, Y. S. Zhang, J. D. Lin, W. C. Lin, X. L. Hsieh, C. R. Lee, *Adv. Opt. Mater.* **2021**, *9*, 2100746.

[21] B. A. Kowalski, V. P. Tondiglia, K. M. Lee, D. R. Evans, T. J. White, M. S. Mills, *Opt. Express* **2019**, *27*, 16571.

[22] C. T. Xu, P. Chen, Y. H. Zhang, X. Y. Fan, Y. Q. Lu, W. Hu, *Appl. Phys. Lett.* **2021**, *118*, 151102.

[23] a) P. G. De Gennes, *Solid State Commun.* **1968**, *6*, 163; b) R. B. Meyer, *Appl. Phys. Lett.* **1968**, *12*, 281.

[24] V. Borshch, Y. K. Kim, J. Xiang, M. Gao, A. Jakli, V. P. Panov, J. K. Vij, C. T. Imrie, M. G. Tamba, G. H. Mehl, O. D. Lavrentovich, *Nat. Commun.* **2013**, *4*, 2635.

[25] D. Chen, J. H. Porada, J. B. Hooper, A. Klittnick, Y. Shen, M. R. Tuchband, E. Korblova, D. Bedrov, D. M. Walba, M. A. Glaser, J. E. Maclennan, N. A. Clark, *Proc. Natl. Acad. Sci. U. S. A.* **2013**, *110*, 15931.

[26] J. Xiang, Y. Li, Q. Li, D. A. Paterson, J. M. Storey, C. T. Imrie, O. D. Lavrentovich, *Adv. Mater.* **2015**, *27*, 3014.

[27] C. L. Yuan, W. B. Huang, Z. G. Zheng, B. H. Liu, H. K. Bisoyi, Y. N. Li, D. Shen, Y. Q. Lu, Q. Li, *Sci. Adv.* **2019**, *5*, eaax9501.

[28] P. Chen, B. Y. Wei, W. Hu, Y. Q. Lu, *Adv. Mater.* **2020**, *32*, 1903665.

[29] L. Allen, M. W. Beijersbergen, R. Spreeuw, J. Woerdman, *Phys. Rev. A* **1992**, *45*, 8185.

[30] J. Wang, J. Y. Yang, I. M. Fazal, N. Ahmed, Y. Yan, H. Huang, Y. Ren, Y. Yue, S. Dolinar, M. Tur, *Nat. Photonics* **2012**, *6*, 488.

[31] B. Y. Wei, P. Chen, W. Hu, W. Ji, L. Y. Zheng, S. J. Ge, Y. Ming, V. Chigrinov, Y. Q. Lu, *Sci. Rep.* **2015**, *5*, 17484.

[32] V. Denisenko, V. Shvedov, A. S. Desyatnikov, D. N. Neshev, W. Krolikowski, A. Volyar, M. Soskin, Y. S. Kivshar, *Opt. Express* **2009**, *17*, 23374.

[33] C. Provenzano, P. Pagliusi, G. Cipparrone, *Appl. Phys. Lett.* **2006**, *89*, 121105.

[34] Y. H. Lee, K. Yin, S. T. Wu, *Opt. Express* **2017**, *25*, 27008.

[35] M. Khorasaninejad, F. Capasso, *Science* **2017**, *358*, 6367.

[36] H. Wu, W. Hu, H. C. Hu, X. W. Lin, G. Zhu, J. W. Choi, V. Chigrinov, Y. Q. Lu, *Opt. Express* **2012**, *20*, 16684.

[37] W. Ji, C. H. Lee, P. Chen, W. Hu, Y. Ming, L. Zhang, T. H. Lin, V. Chigrinov, Y. Q. Lu, *Sci. Rep.* **2016**, *6*, 25528.

© 2022 Wiley-VCH GmbH

21951071, 2022, 19, Downloaded from https://advanced.onlinelibrary.wiley.com/doi/10.1002/adom.202201088 by Nanjing University, Wiley Online Library on [13/05/2025]. See the Terms and Conditions (https://onlinelibrary.wiley.com/terms-and-conditions) on Wiley Online Library for rules of use; OA articles are governed by the applicable Creative Commons License